Int J CARS (2015) 10:1269–1277
DOI 10.1007/s11548-014-1134-5

ORIGINAL ARTICLE

Automatic segmentation of the nasal cavity and paranasal sinuses from cone-beam CT images

Nhat Linh Bui · Sim Heng Ong · Kelvin Weng Chiong Foong

Received: 13 July 2014 / Accepted: 21 November 2014 / Published online: 12 December 2014

Abstract
Purpose A patient-specific upper airway model is important for clinical, education, and research applications. Cone-beam computed tomography (CBCT) is used for imaging the upper airway but automatic segmentation is limited by noise and the complex anatomy. A multi-step level set segmentation scheme was developed for CBCT volumetric head scans to create a 3D model of the nasal cavity and paranasal sinuses.
Methods Gaussian mixture model thresholding and morphological operators are first employed to automatically locate the region of interest and to initialize the active contour. Second, the active contour driven by the Kullback–Leibler (K–L) divergence energy in a level set framework to segment the upper airway. The K–L divergence asymmetry is used to directly minimize the K–L divergence energy on the probability density function of the image intensity. Finally, to refine the segmentation result, an anisotropic localized active contour is employed which defines the local area based on shape prior information. The method was tested on ten CBCT data sets. The results were evaluated by the Dice coefficient, the volumetric overlap error (VOE), precision, recall, and F-score and compared with expert manual segmentation and existing methods.
Results The nasal cavity and paranasal sinuses were segmented in CBCT images with a median accuracy of 95.72 % [93.82–96.72 interquartile range] by Dice, 8.73 % [6.79–12.20] by VOE, 94.69 % [93.80–94.97] by precision, 97.73 % [92.70–98.79] by recall, and 95.72 % [93.82–96.69] by F-score.
Conclusion Automated CBCT segmentation of the airway and paranasal sinuses was highly accurate in a test sample of clinical scans. The method may be useful in a variety of clinical, education, and research applications.

Keywords Upper airway · Cone-beam CT · Anisotropic localized active contour · Automatic segmentation · Kullback–Lebler divergence · Nasal cavity · Paranasal sinuses

Introduction

The human upper airway is that part of the anatomy associated with the nose, mouth, and vocal tract, including the pharyngeal airway, laryngeal airway, and adjacent structures (Fig. 1). Disorders of the upper airways, such as nasopharyngeal cancer (NPC) [1], obstructive sleep apnea (OSA) [2] and rhinosinusitis [3], are widespread. Cone-beam CT (CBCT) is a promising modality for capturing images of the human upper airway. Although different thin bones structures and soft tissues in CBCT images are poorly discriminated, the boundaries between empty spaces and soft tissues or bones are well defined [4]. Compared with other 3D medical imaging modalities, it offers many advantages such as higher resolution, smaller machine size, and lower cost. The radiation dose of CBCT at 68-368 μSv [5] is significantly lower than that of conventional CT at 994-1160 μSv [6]. Furthermore,

Electronic supplementary material The online version of this article (doi:10.1007/s11548-014-1134-5) contains supplementary material, which is available to authorized users.

N. L. Bui (✉) · S. H. Ong
Department of Electrical and Computer Engineering, National University of Singapore, Singapore, Singapore
e-mail: g0800578@nus.edu.sg

K. W. C. Foong
Faculty of Dentistry, National University of Singapore, Singapore, Singapore

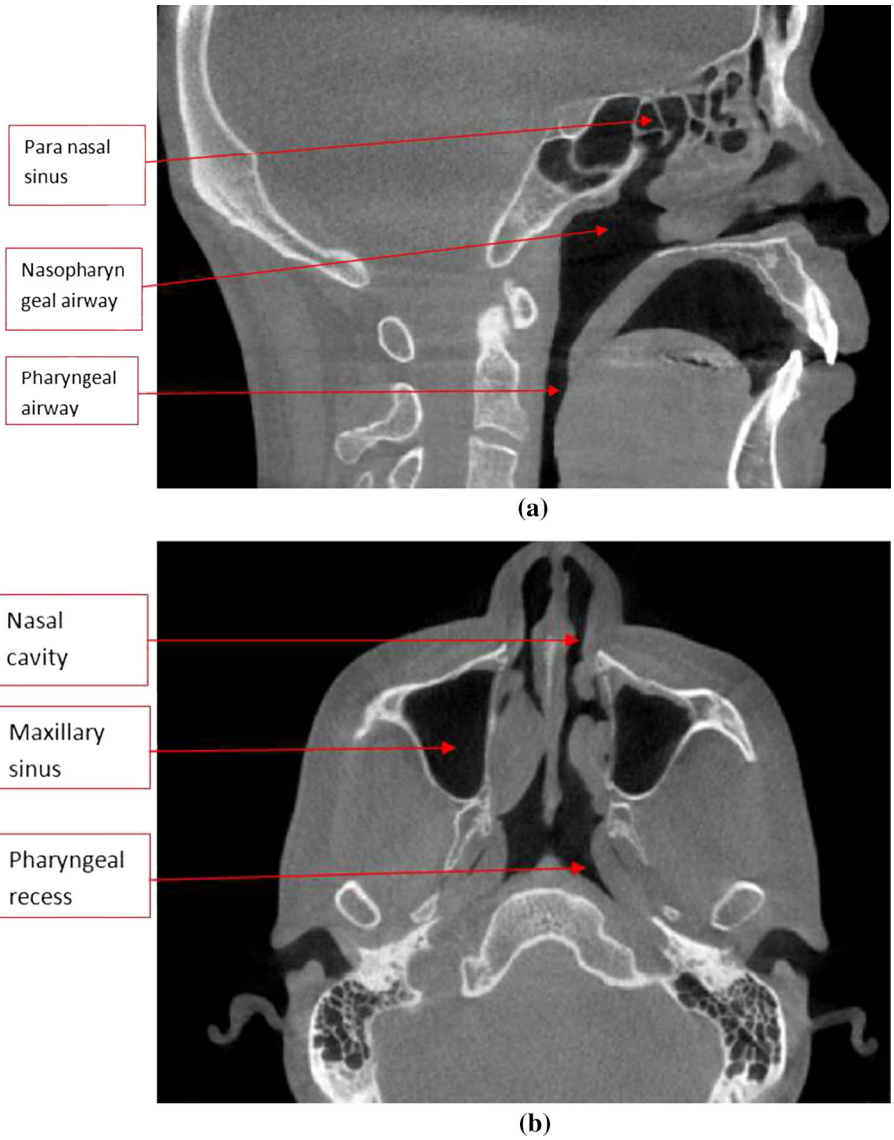

Fig. 1 Anatomy of the upper airway. Images are extracted from one of our data sets

CBCT imaging of the lateral pharyngeal recess, where most NPCs originate, with the subject in the upright position is found to be preferable to multi-detector helical CT imaging with the subject in the supine position [7].

To create a suitable patient-specific 3D model of the human upper airway from CBCT images, accurate image segmentation is required. Since slice by slice manual image segmentation is time consuming and tedious, an automated method is more desirable. The automatic segmentation of the upper airway region including the nasal cavity and paranasal sinuses from CBCT images can be very challenging due to noise, artifacts [8] and the complex anatomical structure. The noise and poor contrast of a CBCT paranasal sinuses image compared with a conventional CT image can be seen in Fig. 2. In recent years, researchers have documented various methods for the automated or semi-automated segmentation of the upper airway from CBCT [9]. Thresholding methods [10–12] were widely used, but they are not sufficient to handle the prominent noise and artifact, especially in the segmentation of the nasal passage region [13,14]. Furthermore, the threshold may have to be changed manually

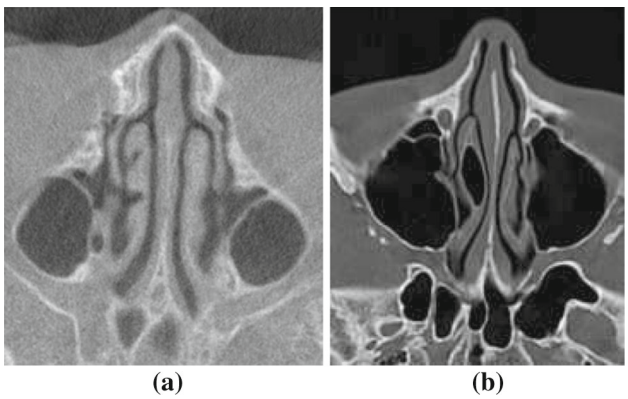

Fig. 2 Comparison of CBCT (**a**) and CT image (**b**)

for different data sets. Another disadvantage is that users have to set the region of interest interactively. There are several approaches [15,16] based on edge-based active contour which are sensitive to noise and weak edges, and the contour must be initialized close to the object boundary. Most of the above work was applied only to the pharyngeal upper airway and did not include the nasal cavity and the paranasal sinuses.

In this study, we present a multi-step scheme for the automated segmentation and reconstruction of the nasal cavity and paranasal sinuses from CBCT images by employing a coarse-to-fine active contour model [17]. We use the Kullback–Leibler (K–L) [18] divergence as the region-based energy to drive the active contour toward the upper airway boundary during the coarse segmentation. We propose a new approach to handle the asymmetry of K–L divergence to directly minimize K–L divergence of the image intensity probability density function. Localized region-based active contour [19] is a method designed to handle image intensity inhomogeneity. During the proposed fine segmentation, a novel anisotropic localized region-based active contour is introduced to refine the coarse segmentation.

Materials and methods

Materials

Approval for using CBCT images of adult patients was given by the National Healthcare Group Domain Specific Review Board. Subsequent image processing and modeling of the paranasal sinus and nasal cavities have been approved by the National University of Singapore Institutional Biosafety Committee. All persons gave their informed consent prior to their inclusion in the study. The CBCT images were anonymized and stored on a different PC for algorithm development and testing. We have managed to obtain ten CBCT data sets of the upper airway that includes the nasal cavity and paranasal sinus. Four data sets are obtained using an i-CAT scanner with 0.25 mm $\times$ 0.25 mm $\times$ 0.25 mm spatial resolution, 640 $\times$ 640 image, at 120 kVp and 5 mAs. The other six data sets are obtained using a Kavo 3D eXam scanner with 0.2 mm $\times$ 0.2 mm $\times$ 0.2 mm spatial resolution, 416 $\times$ 416 image, at 85 kVp and 5 mAs. The images are stored as DICOM file sets.

Methods

The system flowchart is shown in Fig. 3. The input is a CBCT data set of the human head, and the output is the 3D virtual model of the nasal cavity and paranasal sinuses. Automatic thresholding and morphological operations [20] are

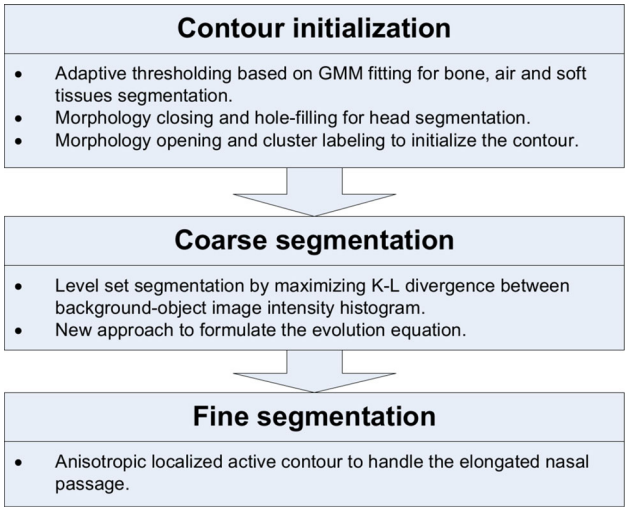

Fig. 3 Flow chart of the nasal cavity and paranasal sinuses segmentation scheme

employed to estimate the region of interest and the initial contour. The proposed coarse-to-fine region-based active contour is then applied to evolve the initial contour to the desired boundary.

Region of interest estimation and contour initialization

We propose an automated method for identifying the ROI. In the first step, adaptive thresholding based on Gaussian mixture model (GMM) fitting is employed to delineate the head shape. Morphological operators are applied to close the openings, fill up the airway, remove the noise, and initialize the contour. Detailed methods are in the Supplementary Materials.

Level set segmentation

We propose a coarse-to-fine level set segmentation scheme to delineate the nasal cavity and paranasal sinus. In our coarse segmentation phase, K–L divergence is employed as the energy. In the fine segmentation phase, we implement the anisotropic localized active contour. The method is described in the Supplementary Materials.

Implementation

We implement the segmentation scheme in Matlab and C++. Details are in the Supplementary Materials.

Evaluation method

The manual segmentations (ground truth) of the nasal cavity and paranasal sinuses are performed by a clinician with more than 10 years experience. The proposed method is verified

by comparing the automatic segmentation results with the manual segmentation results. We use five segmentation performance metrics, the Dice coefficient (DC), the volumetric overlap error (VOE), precision, recall, and F-score to evaluate our segmentation result. The Dice coefficient and volumetric overlap error are based on true-positive (TP), false-positive (FP), true-negative (TN), and false-negative (FN) values. DC measures the ratio between the volume of the correctly segmented airway and the total volume of ground truth and the segmented airway. As DC is an agreement measure, a larger number indicates a better match to the ground truth. Volumetric measurement is a popular metric of upper airway segmentation [9] but may not give a true measure of segmentation accuracy as under-segmentation and over-segmentation compensate each other to some extent. Hence, VOE, which measures the ratio between the non-overlap volume and the volumes of both ground truth and the segmented airway, is preferred. To further investigate under-segmentation and over-segmentation, precision and recall can be used. Precision is the fraction of the segmented volume that is correct. Recall is the fraction of the ground truth which is segmented. F-score, the harmonic mean of precision and recall, can be used as a combination of precision and recall. The performance metrics are defined as follows:

$$\mathrm{TP} = \frac{|V(C) \cap V(O)|}{V(O)} \tag{1}$$

$$\mathrm{FP} = \frac{|V(C) \cup V(O) - V(O)|}{V(O)} \tag{2}$$

$$\mathrm{FN} = \frac{|V(C) \cup V(O) - V(C)|}{V(O)} \tag{3}$$

$$\mathrm{TN} = \frac{|\Omega - V(O) - V(C)|}{|\Omega - V(O)|} \tag{4}$$

$$\mathrm{VOE} = \frac{\mathrm{FP} + \mathrm{FN}}{\mathrm{TP} + \mathrm{FN} + \mathrm{TP}} \tag{5}$$

$$\mathrm{DC} = \frac{2\mathrm{TP}}{2\mathrm{TP} + \mathrm{FP} + \mathrm{FN}} \tag{6}$$

$$\mathrm{Precision} = \frac{\mathrm{TP}}{\mathrm{TP} + \mathrm{FP}} \tag{7}$$

$$\mathrm{Recall} = \frac{\mathrm{TP}}{\mathrm{TP} + \mathrm{FN}} \tag{8}$$

$$F\text{-score} = 2\frac{\mathrm{precision} \times \mathrm{recall}}{\mathrm{precision} + \mathrm{recall}} \tag{9}$$

where $V(O)$ is the ground truth volume, and $V(C)$ is the segmentation result volume.

The median and the 25th and 75th quartiles of above metrics are calculated to compare the segmentation accuracy of the proposed method with three relevant methods: Chan–Vese level set (CVL), localized Chan–Vese level set (LCVL) [19], and Bhattacharyya distance level set (BDL) [21]. CVL is the most popular region-based level set image segmentation method. Similar to our method, BDL expands the region-based active contour by using the histogram distance as energy. LCVL handles the image intensity inhomogeneity by localizing Chan–Vese energy which we improve with the anisotropic local area. To test the statistical significance improvement of our method, the Wilcoxon signed-rank test on Dice, VOE, and F-score are performed for each pair of our method and the above methods.

Experimental results

Qualitative results

The results demonstrate the ability of the proposed algorithm to segment objects in noisy images with highly irregular shapes, such as the paranasal sinuses (Fig. 4a–f) and the narrow and long nasal passages (Fig. 4g–i). In Fig. 5, we illustrate the improved segmentation by using the anisotropic local area to help the contour to expand in the direction of the anteroposterior axis (Fig. 5c). In contrast, the isotropic localized active contour is trapped in an incorrect position (Fig. 5b).

We show the 3D upper airway surface model reconstructed from our segmentation results in Figs. 6 and 7. The volumetric segmentation result is transformed to the 3D mesh by applying the marching cube algorithm [22]. We present both the external view as well as the interactive fly-through images. Figure 6 shows the 3D surface model of the paranasal sinus and nasal cavity. The image in Fig. 7 gives the 3D visualization of the pharyngeal recess.

The proposed segmentation scheme exploits the strengths of both the global and localized region-based active contour. The global region-based active contour is less sensitive to initialization but does not perform well when there is inhomogeneity in the image. The localized region-based active contour can deal with inhomogeneity but is required to be initialized close to the boundary if the object's shape topology is complex. Figure 8c shows that our method can handle images with inhomogeneous intensity and complex shapes. Figure 8d shows that the localized region-based active contour [19] fails to segment the thin walls between the small paranasal sinuses. Figure 8e–f illustrates the case when the global region-based active contours [21,23] miss some regions of the airway because of the image inhomogeneity. Original image and manual segmentation are shown in Fig. 8a, b, respectively.

Quantitative result

Our results are compared with three relevant methods: CVL, LCVL, and BDL. The quantitative segmentation performances for each method are presented in Table 1. The median accuracy of the proposed method is 95.72 % [93.82–96.72

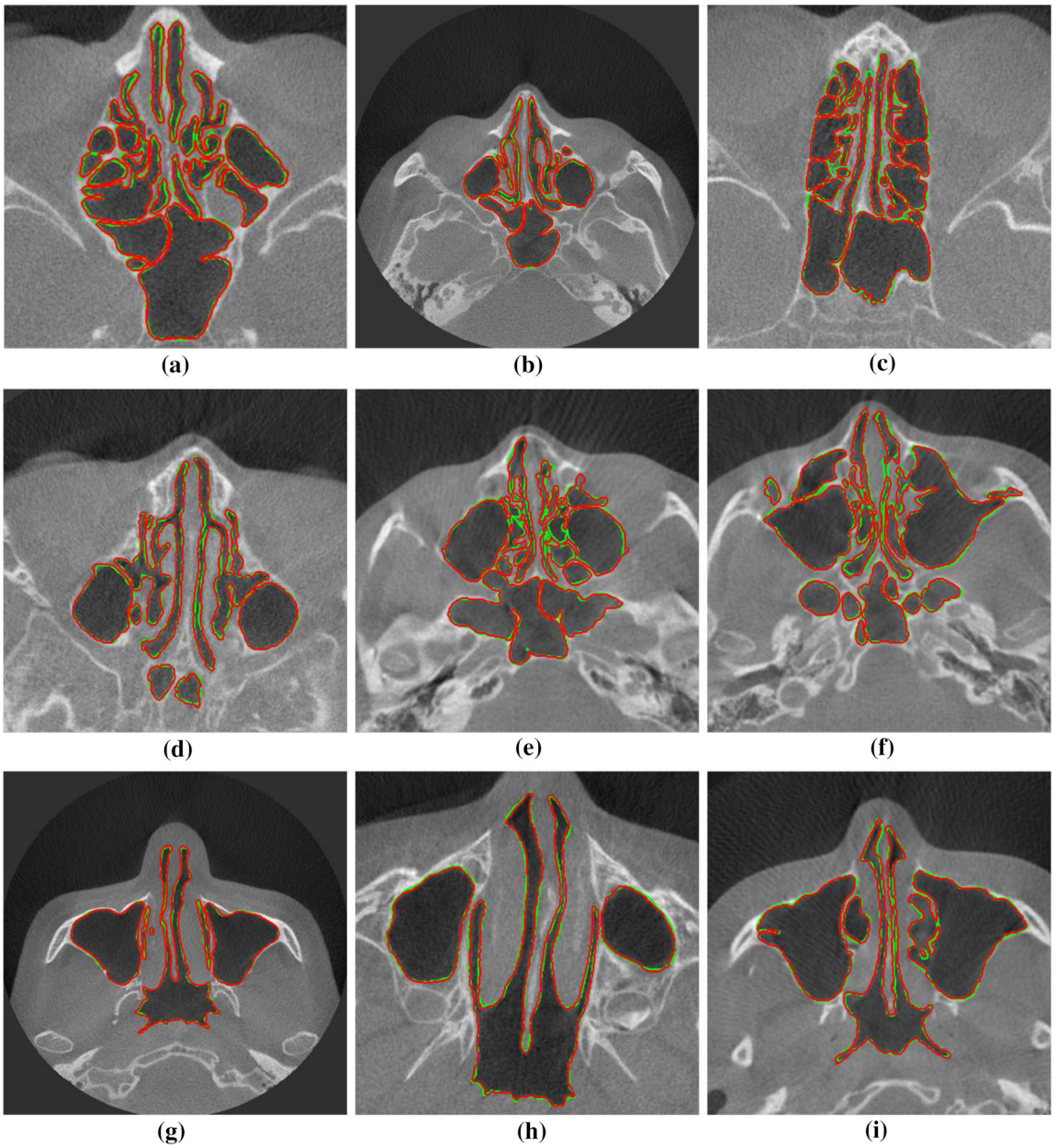

Fig. 4 Segmentation of the paranasal sinuses (**a**)–(**f**) and nasal cavity (**g**)–(**i**). The images are from three subjects, for each subject, three slices from various regions are displayed in order: (**a**, **b**, **g**); (**c**, **d**, **h**); (**e**, **f**, **i**). The *green contour* is the manual segmentation; the *red contour* is the result of our segmentation scheme

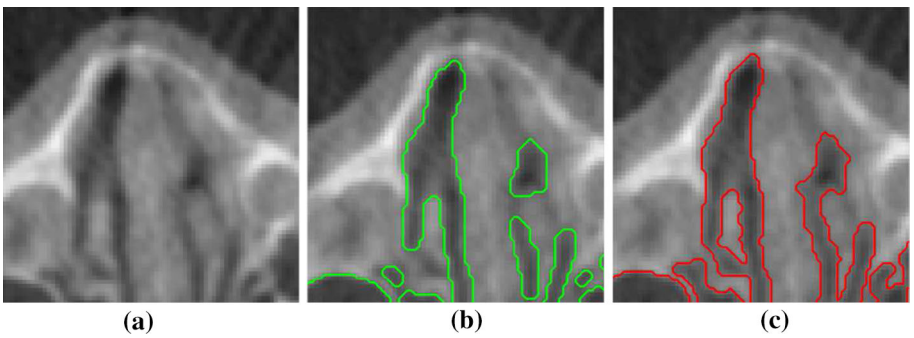

Fig. 5 Comparison between anisotropic and isotropic localized region-based active contour: original image (**a**); isotropic localized active contour result (**b**); anisotropic localized active contour result (**c**)

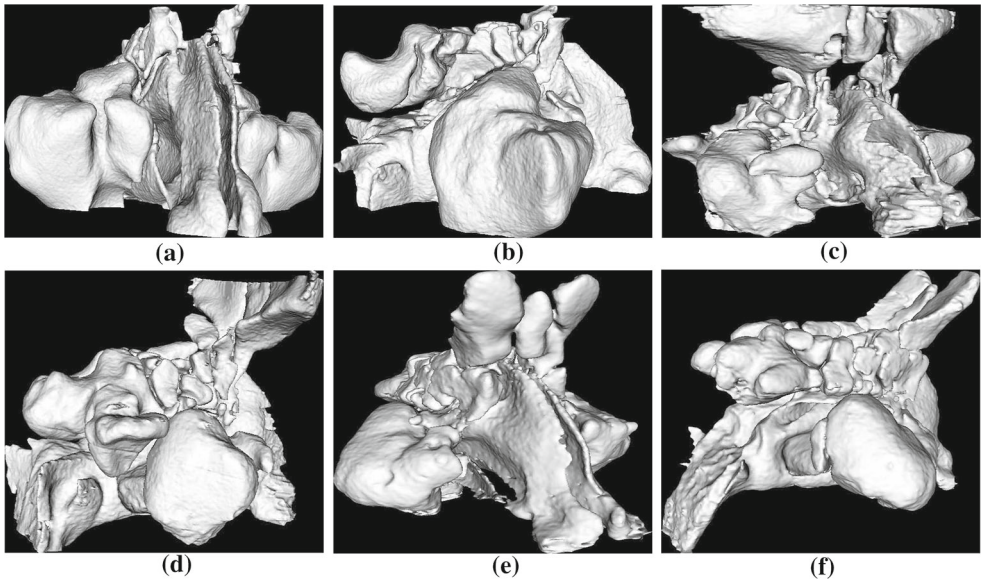

Fig. 6 The 3D surface models of the nasal cavity and paranasal sinus from three data sets. For each subject, two images from different views are displayed in order: (**a**, **b**); (**c**, **d**); (**e**, **f**)

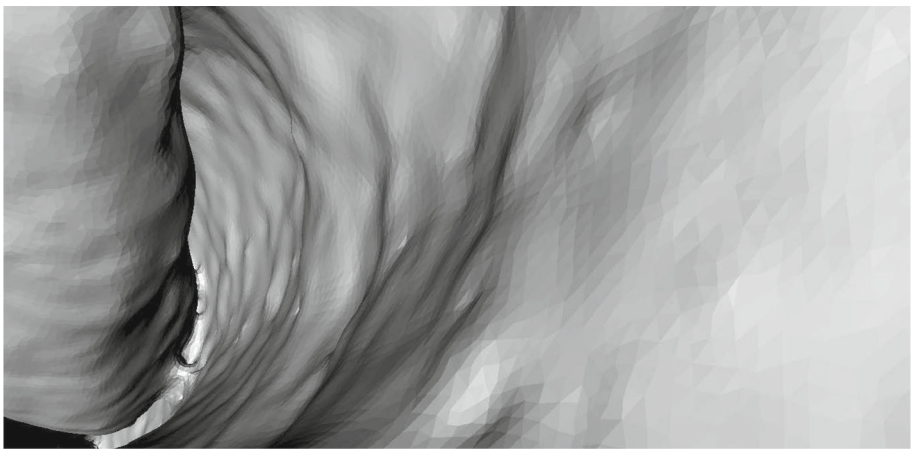

Fig. 7 The 3D surface model of the pharyngeal recess in application of virtual fly-through. Pharyngeal recess is the position where most NPCs originate

interquartile range] by Dice, 8.73 % [6.79–12.20] by VOE, 94.69 % [93.80–94.97] by precision, 97.73 % [92.70–98.79] by recall, and 95.72 % [93.82–96.69] by F-score. Since segmentation accuracy value of our method is higher in each of the ten data sets, nine runs of Wilcoxon signed-rank test on three pairs compared by Dice, VOE, and F-score produce the same result. The tests show that our method has higher accurate segmentation with $Z = 2.694$, exact $p = 0.004$, asymptotic $p = 0.007$. However, after Bonferroni correction, only exact p indicates statistically significant difference.

Discussion

Using expert manual segmentation as ground truth, our method is shown to achieve a highly accurate segmentation result because both the global and local information are used. During coarse segmentation, the robustness of the region-based level set method allows the contour to evolve toward the airway boundary, automatically changing topology if necessary. During the fine segmentation phase, the localized active contour helps the contour converge at the desired boundary of the long and narrow nasal passages. If only global region-based level sets [21,23] are employed, the accuracy might be reduced by the inhomogeneous image. On the other hand, if only the localized active contour [19] is applied, the segmentation result would depend on contour initialization. To automate our system, we used classical image processing methods such as thresholding based on GMM fitting and morphological operations to define the ROI and to initialize the active contour. By incorporating all the above features, we were able to build an automated scheme to seg-

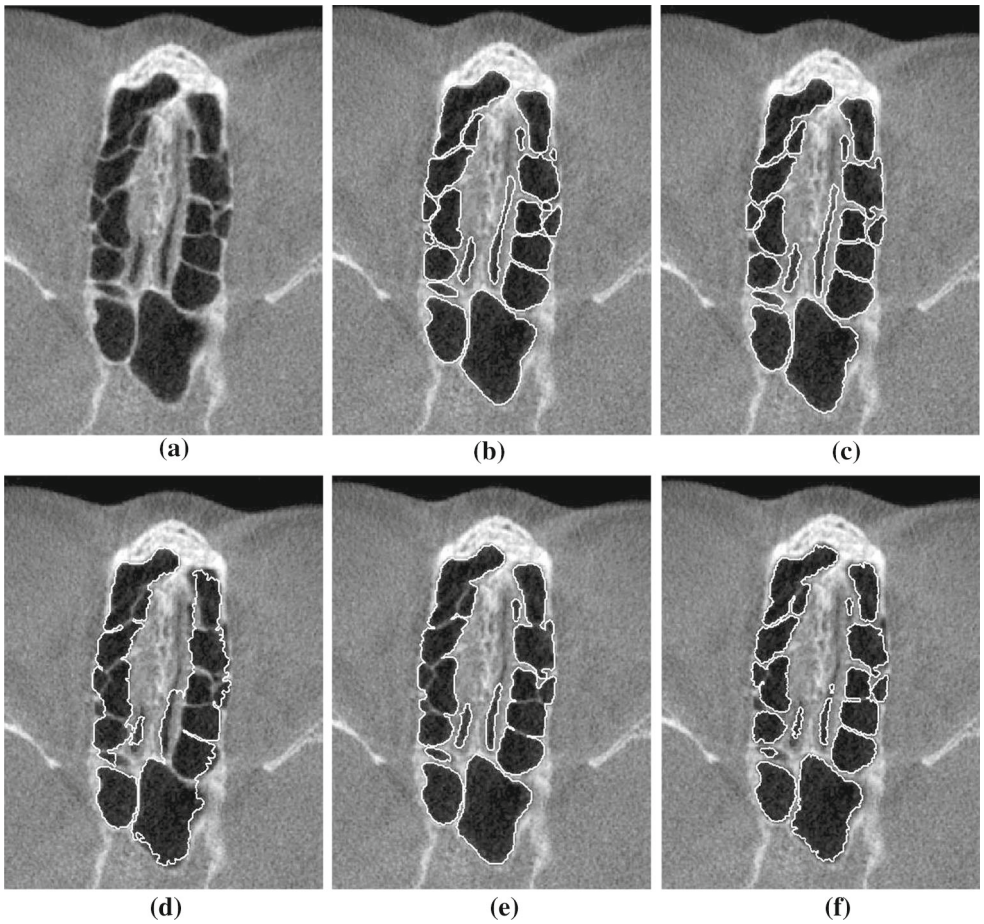

Fig. 8 Visual comparison of paranasal sinuses segmentation between our method (**c**) and other relevant methods: localized region-based active contour (**d**), Chan–Vese level set (**e**), and Bhattacharyya distance level set (**f**). Original image and manual segmentation are shown in (**a**) and (**b**), respectively

Table 1 Segmentation result comparison

	Dice (%)	VOE (%)	Precision (%)	Recall (%)	*F*-score (%)
CVL	94.29 [91.25–94.95]	11.49 [10.38–16.43]	92.65 [92.51–97.56]	94.94 [85.71–97.52]	93.78 [91.25–94.95]
BDL	83.82 [81.74–85.48]	27.96 [23.00–32.01]	99.44 [99.33–99.84]	72.45 [70.11–75-48]	83.83 [82.37–85.78]
LCVL	92.81 [91.33–93.75]	12.78 [12.33–17.46]	96.98 [95.05–97.26]	88.99 [85.85–92.49]	92.81 [91.20–93.75]
Our	95.72 [93.82–96.72]	8.73 [6.79–12.20]	94.69 [93.80–94.97]	97.73 [92.70–98.79]	95.72 [93.82–96.69]

Data are presented as median [interquartile range]

ment and reconstruct the nasal cavity and paranasal sinuses from CBCT images.

Our method achieves a balance between precision and recall as indicated by the *F*-score. If a method gives a result with high precision but low recall, this suggests under-segmentation of the nasal cavity and paranasal sinuses. Such under-segmentation may result in a failure to detect the narrow links between sinuses. It may also result in wrongly detecting blockages of the nasal passage where none exists.

In the coarse segmentation phase, our scheme handles the segmentation task with relatively few parameters by maximizing the difference of the entire image intensity histogram. Employing a single statistic such as mean image intensity in [23] is not sufficient due to the strong presence of noise and the complex anatomy of the nasal cavity and paranasal sinus. Maximizing the K–L divergence, as we have done, is equivalent to minimizing the mutual information between the object and background, which is the most desired segmentation outcome assuming that the background and object image contain different information content.

In our segmentation scheme, the localized active contour in fine segmentation benefits from using the coarse segmen-

tation result for initialization. We further improve on it by using an anisotropic local area to segment the long and narrow nasal passage. Consequently, we achieve a highly accurate segmentation result.

The proposed automatic segmentation scheme of nasal cavity and paranasal sinuses is of direct clinical relevance. It will provide an automatic solution for creating the 3D model from CBCT images. The surface model might be helpful for a physician to visualize the upper airway when interpreting the CBCT images. Furthermore, a simulated system for medical training in upper airway related surgery can be built from the surface model. The 3D surface model can also be employed in vocal tract study as the initial static shape. A CBCT airway segmentation scheme will provide extra information in the case of patients who have already undergone CBCT scans for other treatments such as orthodontics without the need of a high radiation dose of MSCT.

Although we have achieved promising results, there are cases where inaccurate segmentation occurs. Due to the partial volume effect, the thin bone in the paranasal sinus sometimes appears in the image with low intensity. Our method can misclassify these bone regions as noise and give an incorrect segmentation as in Fig. 4c. In skull base surgery, a surgeon usually enters by the nose and breaks through the paranasal sinus bones and soft tissues, but must avoid the vital structures [24]. Treatment planning or surgical simulation based on the 3D model created from the incorrect segmentation results would obviously be undesirable. Another shortcoming is that the proposed method has been tested on a relatively small number of data sets. Even though we have obtained a higher accuracy value in every single data set, the Wilcoxon signed-rank tests (asymptotic $p = 0.007$) still indicate the difference is not statistically significant after Bonferroni correction. For clinical use, the accuracy and reliability of our method should be verified with a larger number of data sets.

Conclusion

We have proposed a scheme for automatic segmentation of the nasal cavity and paranasal sinuses from CBCT image. The accuracy from proposed method are shown to be in higher value than the current CBCT segmentation methods such as global or localized region-based active contour. However, the difference, after Bonferroni correction, is only statistically significant with Wilcoxon signed-rank exact test. To improve the segmentation result, a filter to detect the bone may be incorporated in our segmentation scheme. Expanding our scheme to segment, other structures in CBCT images such as bone or teeth are other possibilities for future work.

Conflict of interest There is no conflict of interest in this study.

References

1. Jia W-H, Qin H-D (2012) Non-viral environmental risk factors for nasopharyngeal carcinoma: a systematic review. Semin Cancer Biol 22(2):117–126
2. Young T, Peppard PE, Gottlieb DJ (2002) Epidemiology of obstructive sleep apnea: a population health perspective. Am J Respir Crit Care Med 165(9):1217–1239
3. Lethbridge M, Schiller JS, Bernadel L (2004) Summary health statistics for U.S. adults: National Health Interview Survey, National Center for Health Statistics. Vital Health Stat 10:222
4. Guijarro-Martinez R, Swennen GR (2011) Cone-beam computerized tomography imaging and analysis of the upper airway: a systematic review of the literature. Int J Oral Maxillofac Surg 40(11):1227–1237
5. Pauwels R, Beinsberger J, Collaert B, Theodorakou C, Rogers J, Walker A, Cockmartin L, Bosmans H, Jacobs R, Bogaerts R, Horner K (2012) Effective dose range for dental cone beam computed tomography scanners. Eur J Radiol 81(2):267–271
6. Loubele M, Bogaerts R, Dijck EV, Pauwels R, Vanheusden S, Suetens P, Marchal G, Sanderink G, Jacobs R (2009) Comparison between effective radiation dose of CBCT and MSCT scanners for dentomaxillofacial applications. Eur J Radiol 71(3):461–468 osteoporosis
7. Sutthiprapaporn P, Tanimoto K, Ohtsuka M, Nagasaki T, Konishi M, Iida Y, Katsumata A (2008) Improved inspection of the lateral pharyngeal recess using cone-beam computed tomography in the upright position. Oral Radiol 24:71–75
8. Katsumata A, Hirukawa A, Noujeim M, Okumura S, Naitoh M, Fujishita M, Ariji E, Langlais RP (2006) Image artifact in dental cone-beam CT. Oral Surg Oral Med Oral Pathol Oral Radiol Endod 101:652–657
9. Alsufyani NA, Flores-Mir C, Major PW (2012) Three-dimensional segmentation of the upper airway using cone beam CT: a systematic review. Dentomaxillofac Radiol 41(4):276–284
10. Ogawa T, Enciso R, Shintaku WH, Clark GT (2007) Evaluation of cross-section airway configuration of obstructive sleep apnea. Oral Surg Oral Med Oral Pathol Oral Radiol Endod 103:102–108
11. Celenk M, Farrell ML, Eren H, Kumar K, Singh GD, Lozanoff S (2010) Upper airway detection and visualization from cone beam image slices. J Xray Sci Technol 18:121–135
12. Weissheimer A, de Menezes LM, Sameshima GT, Enciso R, Pham J, Grauer D (2012) Imaging software accuracy for 3-dimensional analysis of the upper airway. Am J Orthod Dentofacial Orthop 142(6):801–813
13. El H, Palomo JM (2010) Measuring the airway in 3 dimensions: A reliability and accuracy study. Am J Orthod Dentofacial Orthop 137:S50.e1–S50.e9
14. Stratemann S, Huang JC, Maki K, Hatcher D, Millere AJ (2011) Three-dimensional analysis of the airway with cone-beam computed tomography. Am J Orthod Dentofacial Orthop 140:607–615
15. Shi H, Scarfe WC, Farman AG (2006) Upper airway segmentation and dimensions estimation from cone-beam CT image datasets. Int J Comput Assist Radiol Surg 1:177–186
16. Cheng I, Nilufar S, Flores-Mir C, Basu A (2007) Airway segmentation and measurement in CT images. In: 29th annual international conference of the IEEE engineering in medicine and biology society'2007. IEEE EMBC, Lyon, France
17. Osher S, Fedkiw R (2003) Level set methods and dynamic implicit surfaces. Springer, Berlin
18. Kullback S, Leibler RA (1951) On information and sufficiency. Ann Math Stat 22(1):79–86

19. Lankton S, Tannenbaum A (2008) Localizing region-based active contours. IEEE Trans Image Process 17(11):1–11
20. Serra JP (1982) Image analysis and mathematical morphology. Academic Press Inc, London
21. Michailovich O, Rathi Y, Tannenbaum A (2007) Image segmentation using active contours driven by the Bhattacharyya gradient flow. IEEE Trans Image Process 16(11):2787–2801
22. Lorensen WE, Cline HE (1987) Marching cubes: a high resolution 3D surface construction algorithm. Comput Graph 21(4):163–169
23. Chan TF, Vese LA (2001) Active contours without edges. IEEE Trans Image Process 10(2):266–277
24. Trvillot V, Sobral R, Dombre E, Poignet P, Herman B, Crampette L (2013) Innovative endoscopic sino-nasal and anterior skull base robotics. Int J Comput Assist Radiol Surg 8(6):977–987